

# Spontaneous Rayleigh–Brillouin scattering of ultraviolet light in nitrogen, dry air, and moist air

Benjamin Witschas,<sup>1,\*</sup> Maria O. Vieitez,<sup>2</sup> Eric-Jan van Duijn,<sup>2</sup> Oliver Reitebuch,<sup>1</sup>  
Willem van de Water,<sup>3</sup> and Wim Ubachs<sup>2</sup>

<sup>1</sup>Deutsches Zentrum für Luft- und Raumfahrt (DLR), Institut für Physik der Atmosphäre, Oberpfaffenhofen, Germany

<sup>2</sup>Laser Centre, Vrije Universiteit (VU), De Boelelaan 1081, 1081 HV Amsterdam, The Netherlands

<sup>3</sup>Physics Department, Eindhoven University of Technology, Postbus 513, 5600 MB Eindhoven, The Netherlands

\*Corresponding author: Benjamin.Witschas@dlr.de

Received 7 April 2010; revised 17 June 2010; accepted 23 June 2010;  
posted 24 June 2010 (Doc. ID 126662); published 27 July 2010

Atmospheric lidar techniques for the measurement of wind, temperature, and optical properties of aerosols rely on the exact knowledge of the spectral line shape of the scattered laser light on molecules. We report on spontaneous Rayleigh–Brillouin scattering measurements in the ultraviolet at a scattering angle of 90° on N<sub>2</sub> and on dry and moist air. The measured line shapes are compared to the Tenti S6 model, which is shown to describe the scattering line shapes in air at atmospheric pressures with small but significant deviations. We demonstrate that the line profiles of N<sub>2</sub> and air under equal pressure and temperature conditions differ significantly, and that this difference can be described by the S6 model. Moreover, we show that even a high water vapor content in air up to a volume fraction of 3.6 vol.% has no influence on the line shape of the scattered light. The results are of relevance for the future spaceborne lidars on ADM-Aeolus (Atmospheric Dynamics Mission) and EarthCARE (Earth Clouds, Aerosols, and Radiation Explorer). © 2010 Optical Society of America

OCIS codes: 280.3640, 280.1310, 290.5830, 300.6390.

## 1. Introduction

Atmospheric remote sensing with lidar (light detection and ranging) relies on scattering of laser light from air constituents such as aerosol and cloud particles and molecules such as N<sub>2</sub> and O<sub>2</sub>. Range-resolved properties of atmospheric clouds and aerosols, atmospheric trace gas concentrations, temperature, density, and wind velocity can be derived. Lidar techniques use laser emission in the infrared, visible, or ultraviolet (UV) spectral region, where the  $\lambda^{-4}$  dependence of the Rayleigh cross section strongly favors short wavelengths in scattering experiments. Raman scattering is associated with molecules and Rayleigh scattering with molecules and particles of

sizes much smaller than the wavelength of the scattered light, while Mie scattering describes scattering from spherical particles of size equal to the wavelength or larger. The terminology Rayleigh scattering is somewhat ambiguous [1] and may refer to the entire scattering intensity, or to the central unshifted Cabannes line and shifted rotational Raman lines, but excluding the vibrational Raman side features [2,3]. In the present paper we cover the entire line shape of the scattered radiation excluding all Raman lines with the term Rayleigh–Brillouin scattering. In the case of spectrally narrow lasers, rotational and vibrational Raman lines can be distinguished, together with the central Rayleigh–Brillouin line, which has a Gaussian shape for very dilute gases. At higher pressures density fluctuations come into play, leading to distinct Brillouin peaks. This results in a significant change in line shape at atmospheric

pressures that no longer can be represented by a Gaussian.

As pointed out by Fiocco and DeWolf in 1968 [4] Brillouin scattering has to be considered when deriving the frequency spectrum of scattered laser light in the atmosphere. They also expressed the need to develop appropriate models to describe the exact line shape of molecular scattering under atmospheric conditions. In the retrieval of optical properties of the atmosphere using a particular airborne high-spectral resolution lidar (HSRL), errors between 3% and 20% can occur for the aerosol backscatter coefficient for unaccounted Brillouin scattering [5] in the case of medium to high aerosol content. The errors are a factor of 2 larger for spaceborne HSRL, as the planned EarthCARE (Earth Clouds, Aerosols, and Radiation Explorer) mission [6]. For Doppler wind lidar (DWL) based on Rayleigh scattering and using direct detection techniques, a systematic, wind speed dependent error in the retrieved wind speed occurs if the scattered frequency spectrum is assumed to be Gaussian and Brillouin scattering is neglected. The wind speed is overestimated by 10% at sea level and still by 3% for 10 km altitude [7,8]. For the future spaceborne wind lidar on the Atmospheric Dynamics Mission ADM-Aeolus [9,10], which requires a systematic error below 0.7%, Brillouin scattering must be taken into account for the wind retrievals [11] up to altitudes of 30 km [7]. A fringe imaging Michelson interferometer operating at 355 nm is proposed for the measurement of wind speed, temperature, density, and particle scattering ratio, but errors up to  $-14$  K for air temperature and  $+5\%$  for density are predicted, if the Gaussian approximation is used [12].

Based on an approximate solution of the linearized Boltzmann equation, Tenti *et al.* [13,14] described a model (from now on called the Tenti S6 model) for the spectral line shape of scattered radiation, that has since then been widely applied for the retrieval of optical properties with HSRL [15–17] and wind speeds with DWL [7,12,18]. Although the Tenti S6 model was developed for gases of a single-component molecular species, and not for gas mixtures such as air, it is considered as the most appropriate model for atmospheric conditions [2,19].

Several laboratory experiments aiming at deriving the Rayleigh–Brillouin line shape have been performed on Ar, Xe, N<sub>2</sub>, CH<sub>4</sub>, and CO<sub>2</sub> [20], on isotopes of hydrogen [21], on N<sub>2</sub> [22,23], on N<sub>2</sub>, CO<sub>2</sub>, C<sub>2</sub>F<sub>6</sub>, C<sub>2</sub>H<sub>6</sub>, and He–Kr mixtures [24], on He, Ne, and Ar [25], on a mixture of He–Ne and He and isotopes of H<sub>2</sub> [26], on Ar, Kr [27], as well as on N<sub>2</sub>, O<sub>2</sub>, and CO<sub>2</sub> [28]. But up to now, no measurements were performed on a mixture of N<sub>2</sub> and O<sub>2</sub> representative of air. Tenti *et al.* [14] compared their S6 model to measurements on the hydrogen molecule and its deuterium containing isotopologues by Hara *et al.* [21], whereas Sandoval and Armstrong compared their N<sub>2</sub> measurements with a line shape model by Sugawara and Yip [29]. Lao *et al.* [24] used N<sub>2</sub> mea-

surements at a pressure of 11000 hPa and CO<sub>2</sub> measurements down to 200 hPa for their comparison to the S6 model. But none of the performed measurements on N<sub>2</sub> at atmospheric conditions were compared to the Tenti S6 model.

In order to quantify precisely the line shape of light scattering in air, there is an urgent need for precise data and validation of commonly used line shape models. In addition, the influence of water molecules on the line shape has to be investigated, as water vapor is the most relevant air constituent among N<sub>2</sub> and O<sub>2</sub> within the lower troposphere. In the past [30,31], water molecules were shown to have a very large influence on sound damping at frequencies from 10 Hz to 100 kHz. It is a question whether this influence extends to the gigahertz frequency range that is relevant for light scattering.

In the present paper we present high-precision Rayleigh–Brillouin scattering experiments on N<sub>2</sub> as well as on dry and water vapor saturated air, and we establish the accuracy of the Tenti S6 model. In contrast to earlier Rayleigh–Brillouin scattering experiments in the visible spectral region, these measurements are performed in the ultraviolet, which is widely used for direct-detection DWL [32,33], including the lidar on ADM-Aeolus and the HSRL on EarthCARE. For technical reasons the present study employs a wavelength of 366 nm and a scattering angle of 90°. In view of the relatively small wavelength difference the results obtained should, after scaling for the wavelength, be applicable for the case of 355 nm, and probably also for other laser wavelengths. However, the frequency dependence of the bulk viscosity should be investigated in that case. Furthermore, after scaling for the scattering angle, the results obtained are also applicable for other scattering angles, for instance, 180° as used in lidar measurements.

## 2. Background

Spontaneous Rayleigh–Brillouin scattering (SRB) in gases originates from thermal density fluctuations. It is called “spontaneous” to distinguish it from a quite recent technique where the density perturbations are induced by optical dipole forces using laser light [27]. The equilibrium fluctuations of a molecular gas come in the form of fluctuations of both kinetic and internal energy and density. The density fluctuations lead to a fluctuating dielectric constant and scattering of light. More precisely, the scattering cross section is proportional to the Fourier transform of the density–density correlation function [34]. The Brillouin side peaks are more pronounced at higher pressures, while their magnitude depends on how strong the density fluctuations are damped. These density fluctuations can be viewed as thermal sound waves, and therefore the magnitude of the Brillouin side peaks depends on how these sound waves are damped. The damping of sound is determined by the heat conductivity, the heat capacity, and the viscosity of the gas.

The influence of density fluctuations on the line shape of the scattered light is largest when the wavenumber of sound matches the size of the scattering wave vector of light,  $k = 2 k_i \sin(\theta/2)$ , where  $k_i$  is the wave vector of the incident beam and  $\theta$  is the scattering angle. Therefore, if  $c_s$  is the velocity of sound, the frequencies where the sound peaks occur in the scattered light frequency spectrum are shifted from the central frequency by  $\Delta f = \pm c_s 2 \sin(\theta/2)/\lambda$ , with  $\lambda$  the wavelength of the incident beam. With  $c_s = (\gamma k_B T/M)^{1/2}$ ,  $M$  as the mass of a molecule,  $\gamma = 1.4$  as the heat capacity ratio when no vibrational degrees of freedom are excited, and  $k_B = 1.38 \times 10^{-23}$  J/K as the Boltzmann constant, the frequency shift is about 1.3 GHz for the typical conditions of our experiment ( $\lambda = 366.5$  nm,  $\theta = 90^\circ$ , and  $T = 300$  K). A few model spectra for different gas conditions are shown in Fig. 1.

For the backscattering of UV light in air at atmospheric pressures, the scattering wavelength becomes of the order of the mean free path between collisions of the molecules. A key parameter is the ratio  $y$  of the scattering wavelength  $2\pi/k$  to the mean free path between collisions [14],

$$y = \frac{p}{k v_0 \eta} = \frac{n k_B T}{k v_0 \eta}, \quad (1)$$

with  $n$  as the number density,  $T$  as the temperature,  $p$  as the pressure,  $v_0$  as the most probable thermal velocity,  $v_0 = (2k_B T/M)^{1/2}$ , and  $\eta$  as the shear viscosity. The definition of  $y$  is based on the dimensional relation between the mean free path between collisions and the shear viscosity  $\eta$ .

For  $y \gg 1$ , the hydrodynamic regime, the mean free path between collisions is much smaller than the scattering wavelength. In that case, the gas

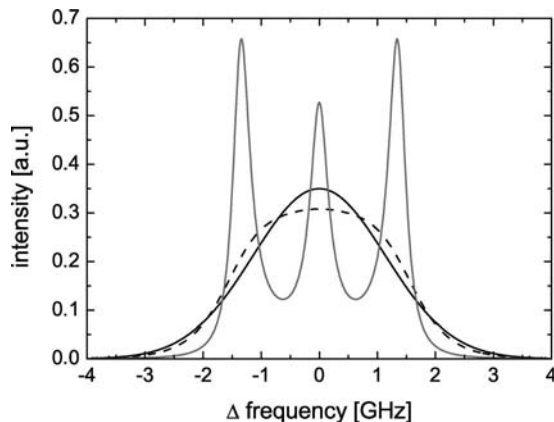


Fig. 1. Line shapes of SRB scattered light according to the Tenti S6 model (wavelength  $\lambda = 366.5$  nm, scattering angle  $\theta = 90^\circ$ ) in nitrogen for different scattering regimes. The black curve is representative for the Knudsen regime ( $y = 0$ , for  $p \approx 0$  hPa,  $T = 293$  K), the dashed black curve for the kinetic regime ( $y = 0.56$ , for  $p = 1000$  hPa,  $T = 293$  K), and the gray curve for the hydrodynamic regime ( $y = 5.6$ , for  $p = 10000$  hPa,  $T = 293$  K). Curves are normalized to yield unity integrated intensity. The gas transport parameters of nitrogen that are used for simulation can be found in Table 1.

can be treated as a continuum, and the spectrum of the scattered light can be calculated using the Navier–Stokes equations. The resulting spectrum can be well approximated by the sum of three Lorentzians displaced by  $\Delta f$  [35]. In the Knudsen regime,  $y \ll 1$ , the mean free path between collisions is much larger than the scattering wavelength. Scattering is solely due to individual thermal molecules, and the line profile is described by the Rayleigh distribution according to

$$I(k, \omega) = \frac{2\pi^{1/2}}{k v_0} e^{-(\omega/k v_0)^2}. \quad (2)$$

In the kinetic regime  $0.3 \lesssim y \lesssim 3$ , which is the relevant regime for atmospheric scattering ( $y \approx 0.1$ – $0.4$  for standard atmospheric conditions [36],  $\lambda = 355$  nm,  $\theta = 180^\circ$ ), neither the individual particle approach nor the continuum approach applies, and one has to resort to solutions of the Boltzmann equation for the density fluctuations [37]. The Boltzmann equation expresses the dynamical behavior of the position–velocity probability density  $f(\mathbf{x}, \mathbf{v}, t)$  of molecules. Moments of  $f(\mathbf{x}, \mathbf{v}, t)$  provide the transport equations of mass, momentum, and energy of continuum physics, together with expressions of the transport coefficients in terms of the collision cross sections. A linear system arises if the deviation of the probability density function from thermal equilibrium is expanded in eigenfunctions of the linear collision operator. A line shape model results after truncation of this expansion to six or seven terms. It was shown in [14] that, from these two truncations, the six-moment model (the Tenti S6 model) provides the superior fit of experimentally measured line shapes. The line shapes for these different cases, calculated by means of the Tenti S6 model, are sketched in Fig. 1.

While the truncation is one element of the model, the other one is the approximation to the linear collision operator, which embodies elastic and inelastic collisions between molecules. As detailed collision cross sections are not available, the collision operator is constructed such that the moments reproduce the known values of the transport coefficients. This reconstruction can be done in several ways. The theory of Taxman [38] describes the internal degrees of freedom of a molecule classically, and the semiclassical theory of Wang-Chang and Uhlenbeck [39] treats those degrees of freedom quantum-mechanically but does not deal with degenerate states. This problem was cured in the model by Waldmann and Snider [40]. The Tenti S6 model uses the collision model of Wang-Chang and Uhlenbeck, which needs the values of shear viscosity, heat conductivity, heat capacity of internal degrees of freedom, and bulk viscosity of the gas under description. The values of these transport coefficients are well documented, except for the bulk viscosity  $\eta_b$ .

The bulk viscosity has its origin in the relaxation of the energy involving internal degrees of freedom of molecules to a change of the kinetic energy. In case

of thermal equilibrium, the internal and the kinetic temperature are the same, but it may take many collisions to equilibrate the two. Therefore, the bulk viscosity depends on the structure of a molecule and is essentially frequency-dependent [41,42]. Wakeham [43] reviewed the status of the study of transport properties of gases and pointed out that the shear viscosity as well as the thermal conductivity can be measured with an accuracy of better than 1% and that data are available for almost all diatomic gases. In contrast to that, the bulk viscosity determination for molecular gases is quite error-prone, which leads to a serious shortage in bulk viscosity data [44]. Practically, there is only one single measurement technique available for bulk viscosity [45], which utilizes sound absorption measurements. However, the errors of this indirect measurement technique are found to range up to 25% or larger [46]. A more grave problem is that these measurements are done at acoustic frequencies (up to  $10^5$  Hz), while light scattering involves frequencies that are four orders of magnitude larger. As the bulk viscosity is strongly frequency dependent, its value at frequencies of the order of gigahertz must be considered largely unknown. In order to establish a value for  $\eta_b$  we will use spontaneous Rayleigh–Brillouin line shape measurements at a pressure of 3000 hPa in combination with the S6 model. As no other measurement technique can reach the high frequencies of light scattering, this is an unavoidable procedure.

The Tenti S6 line shape model is, as for almost all line shape models, restricted to gases consisting of a single species. However, air is a mixture that we will treat as an “effective” medium, consisting of molecules with an effective mass whose collisions are parametrized by effective transport coefficients. Therefore, we shall first present light scattering experiments on pure nitrogen and compare them to the Tenti S6 model, and then compare experiments on air to the S6 model using the effective medium approach. This procedure enables us to estimate the error, which is made by describing the line shape of scattered light in air using the S6 model with transport coefficients of nitrogen, as it was done in the past [5,19]. Furthermore, it gives us the possibility to verify if the line shape prediction is improved if the appropriate transport coefficients (those for air) are used.

We investigate the role of the water vapor content in air, which can reach up to 4 vol.% within the atmosphere (e.g., tropical conditions with water vapor saturated air,  $p = 1013$  hPa,  $T = 30$  °C). Thus, water vapor might be the largest contributor to air after  $N_2$  and  $O_2$ . Water vapor is known to have a large and frequency-dependent influence on the damping of sound. According to sound absorption measurements [30], the bulk viscosity of water vapor saturated air at frequencies of the order of 10 kHz is one order of magnitude larger than that of dry air. These trends are shown in Fig. 2, which shows the bulk viscosity for both water vapor saturated and dry air depending

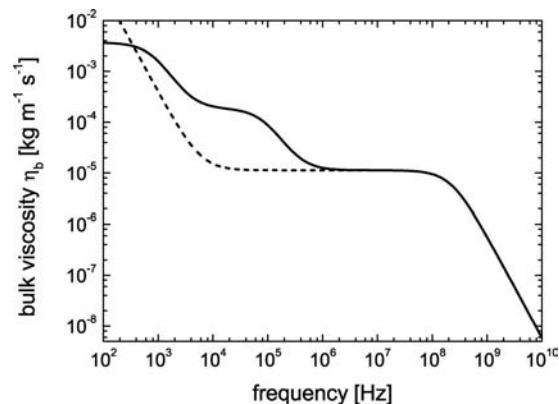


Fig. 2. Bulk viscosity  $\eta_b$  of dry (dashed line) and water-saturated (solid line) air as a function of frequency. The lines represent an empirical formula that is based on sound absorption measurements with sound frequencies up to  $10^5$  Hz [31].

on sound frequency, based on an empirical formula published in [31]. The largest frequency considered in this formula is the rotational relaxation frequency of  $N_2$  and  $O_2$ , after which the bulk viscosity drops to zero. While this might be adequate for the acoustical frequencies for which this formula was designed, it is unrealistic at sound frequencies corresponding to optical wavelengths. Figure 2 also suggests that the influence of water vapor is restricted to low frequencies, but it should be realized that the contribution of the relaxation process at much higher frequencies is not known.

### 3. Experimental Details

A block diagram of the experimental setup used to measure Rayleigh–Brillouin scattering (at Vrije Universiteit, Amsterdam) is shown in Fig. 3. A more detailed description of the experimental setup and instrument specifications can be found in [47,48].

The measured line shape of scattered radiation is the result of the convolution of the real molecular profile and the instrument function, which itself is

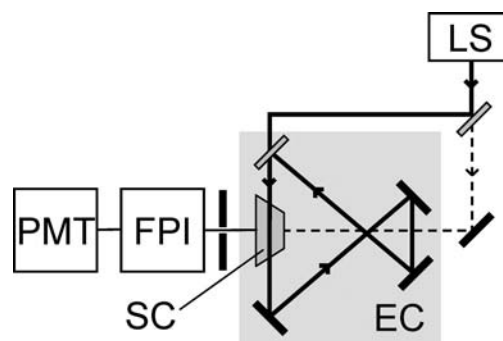


Fig. 3. Schematic diagram of the experimental setup. The UV laser beam (thick solid line), emitted from the laser source (LS), is reflected several times in the enhancement cavity (EC) to increase the scattering intensity. A reference beam (dashed line), split off of the main beam, is used for detector alignment. The in the scattering cell (SC) scattered light (thin solid line) is detected at  $90^\circ$  using a pinhole, a Fabry–Perot interferometer (FPI), and a photomultiplier (PMT).



the result of the convolution of the laser bandwidth and the transmission bandwidth of the Fabry–Perot interferometer. To avoid an influence of the laser bandwidth in the detected signal, a narrowband, continuous wave, single longitudinal mode laser is used. The laser is a titanium sapphire (Ti:Sa) laser that is pumped by a frequency doubled Nd:YVO<sub>4</sub> laser (Millennia), delivering single-mode continuous wave radiation at 732 nm wavelength with an output power of 1.5 W. The laser bandwidth is 1 MHz at 732 nm and the long-term frequency drift is measured with a wavelength meter to be smaller than 10 MHz per hour at 732 nm. After frequency doubling in a nonlinear optical crystal, laser light with a wavelength of 366.5 nm, 2 MHz linewidth, and power of 400 mW is obtained. The UV beam is split to obtain a main beam that is directed into an enhancement cavity and a weaker reference beam that is employed to align the system. The SRB-scattered light is collected at an angle of 90° from an auxiliary focus inside the enhancement cavity, in which a scattering cell (SC) is mounted. The cell is sealed with Brewster windows for not impeding the amplification of the UV circulating power, which reaches a factor of 10, and hence a power level of 4 W at 366.5 nm. The scattering angle is calculated to be 90° ± 0.9° by means of the reference laser beam and geometrical relations using sets of diaphragms and pinholes present in the optical setup. In a few cases, slightly better fits of the model spectra to the measurements could be obtained by selecting the scattering angle  $\theta$  from this interval. The scattered light is filtered by a diaphragm that covers an opening angle of 2°, collected by a set of lenses, further filtered by an extra pinhole ( $d = 50 \mu\text{m}$ ), and is then directed into a scanning Fabry–Perot interferometer (FPI), which is used to resolve the frequency spectrum of the scattered light. The FPI is built as a hemispherical version of a confocal etalon, which means that it is composed of one spherical and one plane mirror [49]. To scan the FPI plate distance, the spherical mirror is mounted on a piezo-electrical translator, controlled by a computer. Despite the lower light gathering in comparison to a plane parallel FPI (composed of two plane mirrors), the hemispherical configuration was chosen because of its insensitivity to small changes in tilt and orientation that can occur during scanning. The transmission function of the FPI, which is the instrument function of the experiment, is described by using the Airy function according to [49,50]

$$T(f) = I_0 \left[ 1 + \left( \frac{2\Gamma_{\text{FSR}}}{\pi\Delta f_{\text{FWHM}}} \right) \sin^2 \left( \frac{\pi}{\Gamma_{\text{FSR}}} f \right) \right]^{-1}, \quad (3)$$

where  $I_0$  is the transmission maximum,  $\Gamma_{\text{FSR}}$  is the free spectral range, and  $\Delta f_{\text{FWHM}}$  is the full width at half-maximum of the transmission curve.  $\Gamma_{\text{FSR}}$ , which is the spectral distance between two intensity maxima, was measured as 7.44 GHz. This is large enough to resolve the spectrum of molecular scattered light in

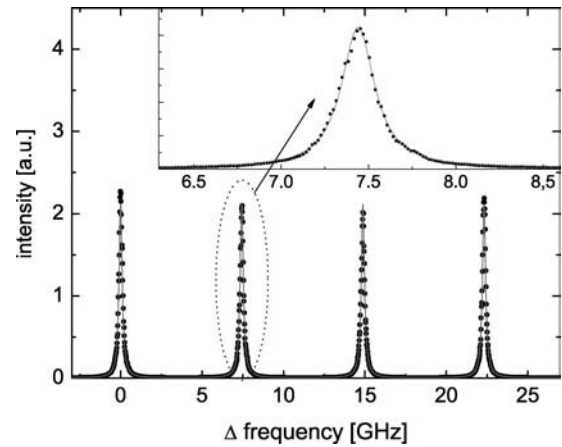


Fig. 4. Transmission curve of the hemispherical FPI versus frequency, obtained with the narrowband reference laser and scanning of the FPI plate separation (black dots), showing three complete free spectral ranges  $\Gamma_{\text{FSR}}$  and details of the instrument function (inset). The gray line represents the best fit of Eq. (3) to the measurement.

the kinetic regime whose FWHM is expected to be about 3–4 GHz for a laser wavelength of 366 nm, pressure values between 300 hPa and 3000 hPa, and temperatures of about 300 K. The  $\Delta f_{\text{FWHM}}$  was determined with Eq. (3) as 232 MHz using a fit to the measured transmission curve (Fig. 4). Throughout, we have used  $T(f)$  to convolve it with the model spectra obtained from the Tenti S6 model. We will indicate the resulting model spectra as  $I_m(f)$ .

The light that passes through the FPI is detected using a photomultiplier tube (PMT) that is operated in the photon-counting mode and read out by a computer. To prevent contamination on the mirrors that could lead to absorption of UV light, the enhancement cavity as well as the FPI is flushed with N<sub>2</sub>. To measure and monitor temperature, pressure, and humidity of the gas under investigation, several measurement devices are mounted in the system. The pressure is measured with two different barotrons, an active capacitive transmitter (Pfeiffer-CMR) for pressure values between 100 and 1000 hPa, and an active piezotransmitter (Pfeiffer-APR) for pressure values between 1000 and 11000 hPa. The temperature is measured with a thermoresistor Pt100, and the humidity with a monolithic integrated circuit with integral thermistor (Honeywell HIH-4602) delivering an accuracy of 3.5% of the measured relative humidity value.

Before performing a measurement, the scattering cell was evacuated and purged with the working gas, before being charged to the desired pressure, to avoid any contamination from gases of previous measurements. The temperature for all measurements ranged between 295 K and 303 K. Pressures between 300 hPa and 3000 hPa were applied. The gas representative for air was a mixture of 79 vol.% N<sub>2</sub> and 21 vol.% O<sub>2</sub>.

As the light-scattering experiments do not provide an absolute intensity, the experimental and model

spectra were normalized such that  $\int_{f_b}^{f_b} I(f)df = 1$ . Ideally, the bounds  $f_b$  of the integration should be such that intensity is zero at  $f = f_b$ ; however, the free spectral range of the etalon is not much larger than the width of the measured spectra. Therefore, we take  $f_b = f_{\text{fsr}}/2$  in the normalization.

Another problem is the signal background  $I_{e_0}$  in the experiment, which must be subtracted from the raw measured spectrum  $I_e(f)$  before normalization of  $I_e(f) = I_e(f) - I_{e_0}$ . It turns out that  $I_{e_0}$  is not just the dark current of the photomultiplier, but also contains a small contribution,  $I'_{e_0}$  of broadband fluorescence of the cell windows. Therefore, it was decided to correct the model spectra  $I_m(f)$  for this poorly known background contribution, by setting  $I_m(f) = aI_e(f) - I'_{e_0}$ , and determining  $I'_{e_0}$  and the proportionality constant  $a$  in a least squares procedure for the wings of the spectra. If the measured spectra would have the correct background,  $a = 1$  and  $I'_{e_0} = 0$ . The wings of the spectra were defined as frequencies such that  $I_m(f) \leq \max(I_m)/4$ . The corrected model spectrum  $I'_m(f) = I_m(f) + I'_{e_0}$  was then normalized again such that  $\int_{f_b}^{f_b} I'_m(f)df = 1$ . This procedure gives a small but perceptible change of the background intensity; it increased the wing intensity  $I_m(f_{\text{fsr}}/2)$  by approximately 25%. In conclusion, in comparing experimental to model line shapes, both the offset and the scale of the vertical axis of the experimental result are chosen to match that of the model spectrum.

Assuming Poisson statistics of the collected photon counts, it is possible to arrive at an estimate of the statistical error  $\sigma(f_i)$  at each (discrete) frequency of the data. This enables us to express the difference between measured spectrum  $I_e(f)$  and modeled spectrum  $I_m(f)$  as a  $\chi^2$  value,

$$\chi^2 = (1/N) \sum_{i=1}^N \frac{I_e(f_i) - I_m(f_i)}{\sigma^2(f_i)}, \quad (4)$$

and thus to quantify the significance of the difference between experiment and model. This is important as the number of photons collected for each spectrum varies and is typically smallest at the lowest pressures.

## 4. Experimental Results

### A. Comparison of N<sub>2</sub> and Air

A key point of this study is the question of how well the Tenti S6 model reproduces the line shape in nitrogen and air, and whether the line shape of spontaneous Rayleigh–Brillouin scattering in air can be explained by using the transport coefficients of nitrogen. Therefore, SRB measurements on N<sub>2</sub> and air at pressure ranges from 300 to 3000 hPa and temperatures of 295.5 to 301 K were performed and compared to the Tenti S6 model.

As explained in Section 2, the value of the bulk viscosity should be considered poorly known at sound frequencies of the order of 1 GHz, at which values

Table 1. Gas Transport Coefficients Used for S6 Model Calculations

		N <sub>2</sub>	Air
Mass number	[g mol <sup>-1</sup> ]	28.013	28.85
Shear viscosity $\eta$	[kg m <sup>-1</sup> s <sup>-1</sup> ]	(1.79 × 10 <sup>-5</sup> ) <sup>a</sup>	(1.846 × 10 <sup>-5</sup> ) <sup>b</sup>
Bulk viscosity $\eta_b$	[kg m <sup>-1</sup> s <sup>-1</sup> ]	(2.2 × 10 <sup>-5</sup> ) <sup>c</sup>	(1.5 × 10 <sup>-5</sup> ) <sup>c</sup>
Thermal conductivity $\kappa$	[W m <sup>-1</sup> K <sup>-1</sup> ]	(25.5 × 10 <sup>-3</sup> ) <sup>a</sup>	(26.24 × 10 <sup>-3</sup> ) <sup>b</sup>
Heat capacity ratio $\gamma$		1.4	1.4

<sup>a</sup>Valid at reference temperature 300 K. Taken from [53].

<sup>b</sup>Valid at reference temperature 300 K. Taken from [52].

<sup>c</sup>Valid at reference temperature 297 K, and frequency 1.3 GHz. Taken from measurements (see Subsection 4.A).

they are relevant for SRB scattering. In order to obtain a value for  $\eta_b$ , we therefore adopted the following procedure: at a pressure of  $p = 3000$  hPa, the influence of Brillouin scattering on the spectrum is large, and therefore its sensitivity to the used value of  $\eta_b$  in the S6 model is large. Therefore, these pressures define a value of  $\eta_b$  at frequencies of about 1.3 GHz, where the S6 model fits the experiment best. This procedure, including the estimate of the uncertainty in the obtained  $\eta_b$ , will be described in a follow-up paper [51]. Summarizing, for N<sub>2</sub> we thus found  $\eta_b = (2.2 \pm 0.5) \times 10^{-5}$  kg m<sup>-1</sup> s<sup>-1</sup>, which is about a factor of 1.7 larger than the literature value of  $1.29 \times 10^{-5}$  kg m<sup>-1</sup> s<sup>-1</sup> [28,44], while for air,  $\eta_b = (1.5 \pm 0.3) \times 10^{-5}$  kg m<sup>-1</sup> s<sup>-1</sup>, which is a factor of about 1.4 larger than the literature value of  $1.1 \times 10^{-5}$  kg m<sup>-1</sup> s<sup>-1</sup> [52]. All transport coefficients used for the model calculations are summarized in Table 1 [52,53].

The measured spectra for N<sub>2</sub> and air at pressures of 2000 and 3000 hPa, the comparison to the Tenti S6 model, and the residuals with respect to the peak intensity are shown in Fig. 5. The corresponding spectra at 3000 hPa were used to establish the value of the bulk viscosity, which was then used for all other model calculations. Significant differences between the S6 model and the measured spectra exist. For N<sub>2</sub> we find  $\chi^2 = 5$  at 2000 hPa and  $\chi^2 = 7$  at 3000 hPa, while for air  $\chi^2 = 9$  at 2000 hPa and  $\chi^2 = 4$  at 3000 hPa. On a relative scale these differences are small; for N<sub>2</sub> at 3000 hPa the error is 3%, and for air at 2000 hPa it is 2.6%.

To clarify further the difference of SRB spectra obtained in pure N<sub>2</sub> and air and to show the capability of predicting this difference using the S6 model, we calculate the residual plots between both spectra (N<sub>2</sub> and air) obtained at almost the same measurement conditions (Table 2). The difference between the N<sub>2</sub> and air spectra is quantified in two ways. First the statistical significance of this difference is illustrated by plotting the normalized frequency-dependent difference,

$$\Delta(f_i) = \frac{I_{\text{N}_2}(f_i) - I_{\text{air}}(f_i)}{(\sigma_{\text{N}_2}(f_i)^2 + \sigma_{\text{air}}(f_i)^2)^{1/2}}, \quad (5)$$

where  $\sigma_{\text{N}_2}$  and  $\sigma_{\text{air}}$  are the statistical errors of the measured N<sub>2</sub> and air spectra assuming Poisson

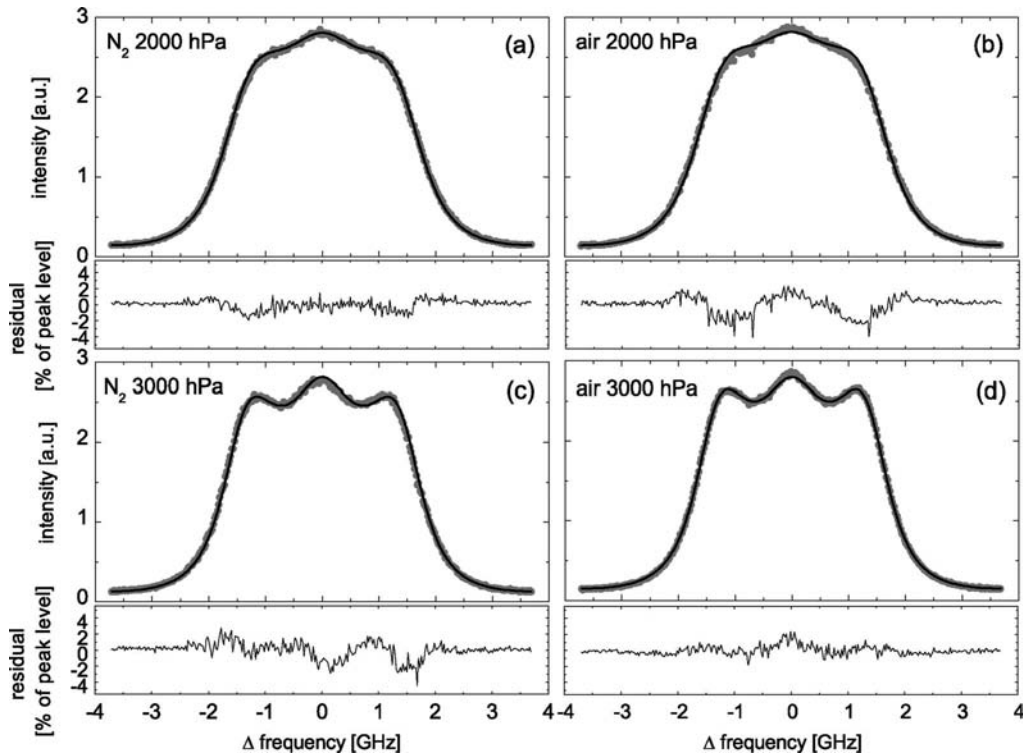


Fig. 5. Measured spontaneous Rayleigh–Brillouin scattering spectra (gray dots) in  $N_2$  (left) and air (right) compared with the S6 model using the transport coefficients in Table 1. Measurement and model are normalized to equal area as described in Section 3. (a)  $N_2$ , 2000 hPa,  $\chi^2 = 5$ . (b) air, 2000 hPa,  $\chi^2 = 9$ . (c)  $N_2$ , 3000 hPa,  $\chi^2 = 7$ . (d) air, 3000 hPa,  $\chi^2 = 4$ . The spectra at 3000 hPa were used to determine the bulk viscosity. Significant discrepancies exist between the Tenti S6 model and the measured spectra for  $N_2$  at 3000 hPa and for air at 2000 hPa. The exact measurement conditions can be found in Table 2.

statistics, respectively. Second, the difference is also presented as a percentage deviation by comparing it to the intensity at  $\Delta f = 0$ . The measured as well as the modeled difference for a 300 hPa (a) and a 2000 hPa measurement (b) is shown in Fig. 6.

It is apparent from Fig. 6 that the spectrum in  $N_2$  differs significantly from that in air down to 300 hPa. The difference is about  $\pm 2\%$  of peak level for both measurements. The difference between  $N_2$  and air spectra can be reproduced well by the Tenti S6 model when taking the corresponding transport coefficients (Table 1). From the gas transport properties that determine the line shape, the molecular mass sets its overall width via the Doppler effect. The other transport coefficients (shear viscosity, bulk viscosity, and

thermal conductivity) have a smaller influence on the line shape. Taking a fictitious gas with the mean molecular mass of air and  $N_2$  transport coefficients, as it was done in [5], produces a line shape at  $p = 3000$  hPa that is indistinguishable from that using all air transport coefficients. The  $\chi^2$  difference with the experiment shown in Fig. 5(d) has the same value for these two cases. Although our experiments thus justify a common practice, there is no reason not to take the proper gas parameters in line shape models.

### B. Air at Atmospheric Pressures

An accurate simulation of the SRB profile is required for several atmospheric lidar applications

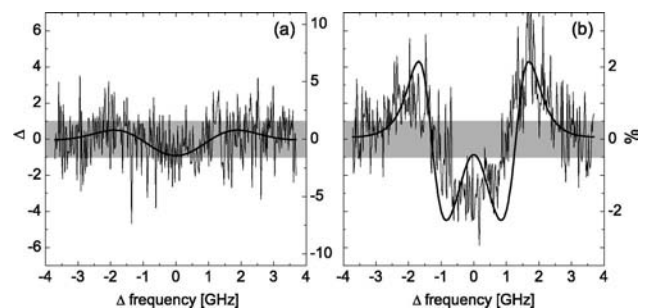


Fig. 6. Normalized difference between measured and modeled SRB line profiles of  $N_2$  and air. Plotted is  $\Delta(f_i)$  [see Eq. (5)] (a) at a pressure of 300 hPa, mean  $\chi^2 = 1.7$  and (b) at 2000 hPa, mean  $\chi^2 = 6.2$ . The right vertical axes give the deviation in percentages; outside the shaded area  $\chi^2 > 1$ .

Table 2. Measurement Conditions and  $y$  Parameter for the SRB Experiments<sup>a</sup>

	$p$ [hPa]	$T$ [K]	$\lambda$ [nm]	$y$	$\theta$
$N_2$	300	298.6	366.501	0.16	90.6°
	2066	295.5	366.514	1.15	89.4°
	3030	296.9	366.512	1.69	89.4°
Dry air	300	298.0	366.510	0.16	90.6°
	504	298.0	366.510	0.28	90.6°
	1040	299.4	366.496	0.57	90.6°
	2015	297.5	366.533	1.11	89.4°
	3050	297.5	366.531	1.65	89.4°
Moist air	1040	301.2	366.496	0.57	90.6°

<sup>a</sup>Measurements are shown in Figs. 5–8.



as discussed in Section 1. It is common that the S6 model with  $N_2$  gas parameters [5,18,19], or even the Gaussian approximation from the Knudsen regime [54–57], are used for this purpose. We already showed in Subsection 4.A that the difference in line shape between air and pure nitrogen is obvious, and can be described with the S6 model. Furthermore, we verify that the Gaussian approximation is not a satisfactory description of SRB line shapes, not even for

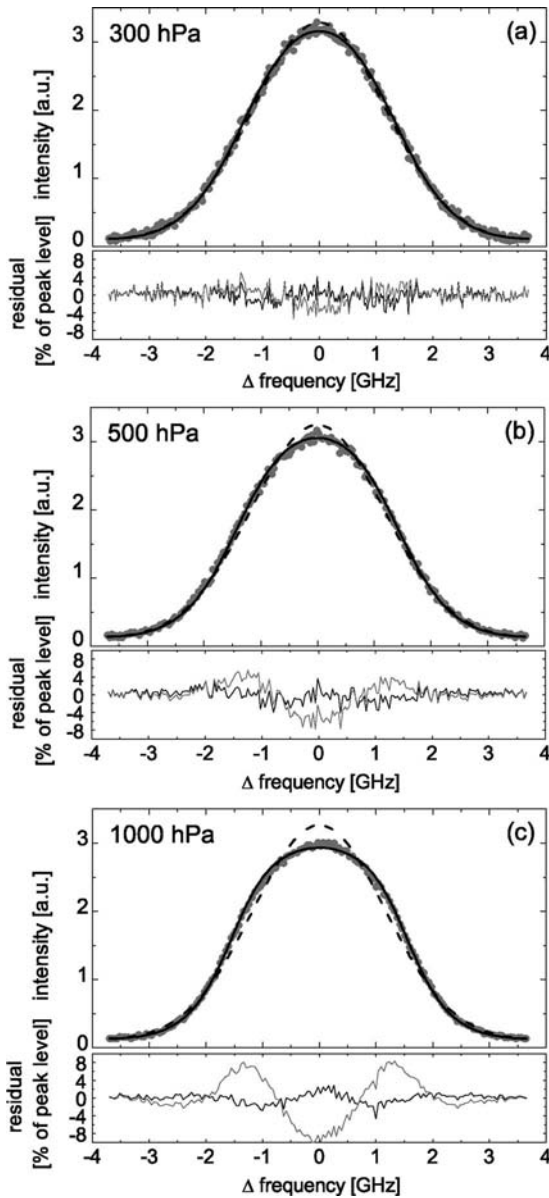


Fig. 7. Measured spontaneous Rayleigh–Brillouin spectra in air (gray dots), compared to the S6 model (full line) and the Rayleigh distribution (dashed line) at pressures of (a)  $p = 300$ , (b) 500, and (c) 1000 hPa. The difference between measurement and S6 model (black) and measurement and Rayleigh distribution (gray) as a percentage deviation compared to the intensity at  $\Delta f = 0$  is shown below each graph. For the Tenti S6 model, the normalized differences between experiment and model are (a)  $\chi^2 = 2.0$ , (b) 2.5, and (c) 3.7. For the Rayleigh distribution, these differences become (a)  $\chi^2 = 2.6$ , (b) 7.6, and (c) 50. The detailed measurement conditions can be found in Table 2.

atmospheric pressures down to 300 hPa, corresponding to an altitude of 10 km above sea level. Figure 7 shows spectra measured in air at 300 (a), 500 (b), and 1000 hPa (c), and the comparison to both the Tenti S6 model and the Gaussian line shape. The model spectra have been convolved with the instrument function [Eq. (3)]. Below each graph, the difference between model and measurement as a percentage deviation compared to the intensity at  $\Delta f = 0$  is shown. The deviation between the S6 model and measurement is about  $\pm 2\%$  for all three cases. On the contrary, the deviation between measurement

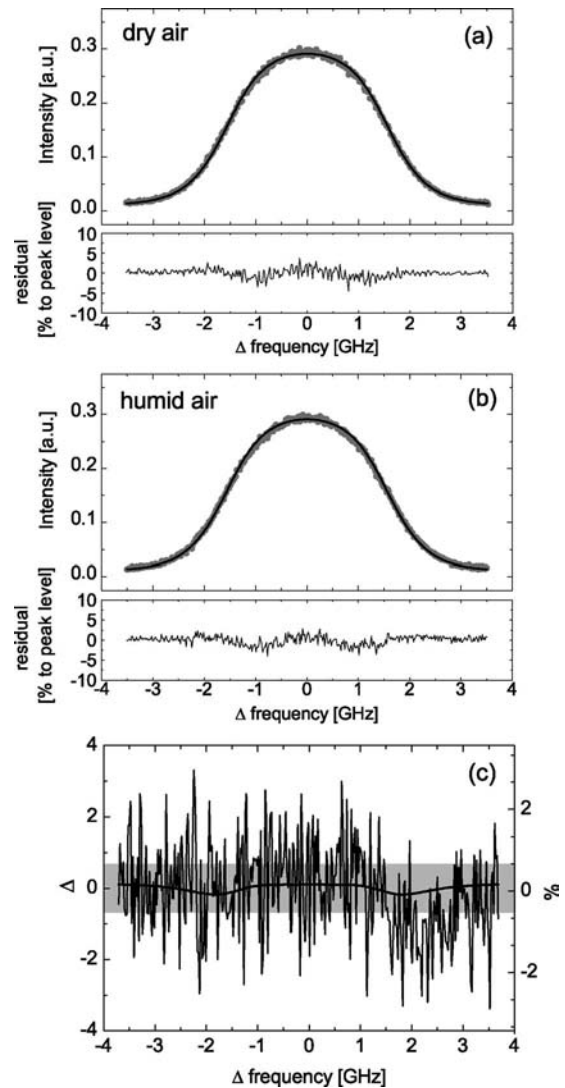


Fig. 8. (a) Measured spectrum of dry air compared to the Tenti S6 model ( $T = 299.4$  K,  $p = 1040$  hPa,  $\theta = 90.6^\circ$ ). The difference between model and data is expressed by  $\chi^2 = 3.1$ . (b) Measured spectrum of water saturated air compared to the Tenti S6 model ( $T = 301.0$  K,  $p = 1040$  hPa,  $\theta = 90.6^\circ$ ). The difference between model and data is expressed by  $\chi^2 = 2.7$ . The difference between model and measurement as a percentage deviation compared to the intensity at  $\Delta f = 0$  is shown below (a) and (b), respectively. (c) Normalized difference  $\Delta$  between measured spectra of (a) and (b), with the mean squared difference  $\chi^2 = 1.7$ ; outside the shaded area  $\chi^2 > 1$ . The right vertical axis indicates the percentage difference.



and Gaussian approximation is about  $\pm 9\%$  for an ambient pressure of 1000 hPa ( $\approx$  sea level), and still about  $\pm 3\%$  for an ambient pressure of 300 hPa ( $\approx$  10 km above sea level). This clearly demonstrates that the Gaussian approximation is inadequate at pressures of 500 and 1000 hPa, while it is still significantly worse than the Tenti S6 model at  $p = 300$  hPa.

### C. Moist Air

As humidity was shown to have a large effect on bulk viscosity at acoustical frequencies, it may also have an effect on scattering line shapes, which correspond to much larger sound frequencies. Therefore, we compared SRB spectra obtained in dry and water vapor saturated air. The relative humidity content was measured to 99.4–99.9% for the case of water vapor saturated air. In both experiments, the temperature was  $[300 \pm 0.25]$  K and the ambient pressure was  $[1040 \pm 5]$  hPa, which corresponds to a volume fraction of water vapor of 3.6%. The result of these experiments is shown in Fig. 8. Both spectra are modeled well by the S6 model, using the transport coefficients of dry air in both cases, while a plot of the normalized difference [Eq. (5)] in Fig. 8(c) does not show a significant difference. Although all transport coefficients are the same when taken at the same reference temperature, the model spectra are slightly different due to the slightly different temperatures of the two experiments. These results show that at gigahertz frequencies, water molecules do not significantly affect the bulk viscosity, at least not for a water vapor content up to 3.6 vol.%, which is almost the upper bound within the atmosphere.

It is remarkable that the disappearance of the influence of water on the bulk viscosity  $\eta_b$  at high frequencies is consistent with Fig. 2. However, since the empirical formula represented by Fig. 2 was designed for acoustic frequencies, this agreement must be deemed fortuitous.

## 5. Summary and Conclusion

Spontaneous Rayleigh–Brillouin scattering was measured at a wavelength of 366.5 nm and a scattering angle of  $90^\circ$ . The measurements were performed for  $N_2$ , dry air, and humid air with temperatures of 295 to 301 K and ambient pressures of 300 to 3000 hPa. For the first time to our knowledge, the SRB line shapes of  $N_2$  and air in the kinetic regime were compared to the Tenti S6 model. The bulk viscosity for frequencies of the order of gigahertz of  $N_2$  and air was determined using SRB measurements at the largest pressure (3000 hPa) in combination with the S6 model. We demonstrate that the line shapes obtained in  $N_2$  and air under the same measurement conditions differ significantly at pressures of 2000 and 300 hPa, and that this difference is mainly caused by the mass difference between  $N_2$  and air. In addition it is shown that the Gaussian approximation is not a satisfactory description for SRB line shapes obtained in air with atmospheric pres-

ures down to 300 hPa. It is further shown that the line shapes of  $N_2$  and air can be described by the Tenti S6 model, with small but measurable discrepancies at atmospheric and higher pressures. However, on a relative scale these deviations are about  $\pm 2\%$  with respect to the peak intensity. We furthermore point out that humidity has no significant influence on the line shape of the scattered light, not even for high water vapor contents up to 3.6 vol.% in the atmosphere.

We have shown that the S6 model, which refers to a single-species molecular gas, can be applied to air by using the effective transport coefficients of air. However, this approach is not physically sound. The Tenti S6 model is a kinetic model that involves collisions between molecules expressed in a single collision integral. Air contains different molecules with different collision cross sections. A better line shape model, therefore, should explicitly involve those details. For gases consisting of hard spheres atoms, such a model was recently designed, and was shown to provide a better fit to spectra of noble gas mixtures than a hydrodynamic model [58]. However, hard sphere molecules have no internal degrees of freedom. Hopefully our results inspire further work on line shape models of mixtures with internal degrees of freedom. A comparison of our data with this and other models will be described in a forthcoming publication [59].

Although we have now established the insignificance of water for SRB line shapes, the influence of other trace gases such as  $CO_2$ ,  $CH_4$ , and Ar of the real atmosphere remains to be investigated.

This work was funded by the European Space Agency (ESA), contract 21396/07/NL/HE. The review and valuable comments by Anne-Grete Straume and Olivier Le Rille are highly appreciated. The research leading to these results has received funding from the European Commission (EC) Seventh Framework Program (FP7/2007-2013) under grant agreement 228334. The core part of the code that computes the S6 model has been kindly provided to us by Xing-guo Pan. Two anonymous reviewers provided very helpful suggestions and comments.

## References

1. A. T. Young, "Rayleigh scattering," *Appl. Opt.* **20**, 533–535 (1981).
2. R. B. Miles, W. R. Lempert, and J. N. Forkey, "Laser Rayleigh scattering," *Meas. Sci. Technol.* **12**, R33–R51 (2001).
3. C. Y. She, "Spectral structure of laser light scattering revisited: bandwidths of nonresonant scattering lidars," *Appl. Opt.* **40**, 4875–4884 (2001).
4. G. Fiocco and B. J. DeWolf, "Frequency spectrum of laser echoes from atmospheric constituents and determination of the aerosol content of air," *J. Atmos. Sci.* **25**, 488–496 (1968).
5. B. Y. Liu, M. Esselborn, M. Wirth, A. Fix, D. B. Bi, and G. Ehret, "Influence of molecular scattering models on aerosol optical properties measured by high spectral resolution lidar," *Appl. Opt.* **48**, 5143–5153 (2009).

6. European Space Agency, "Earth Clouds, Aerosols, and Radiation Explorer," ESA SP-1279(1) (European Space Research and Technology Centre, 2004).
7. A. Dabas, M. Denneulin, P. Flamant, C. Loth, A. Garnier, and A. Dolfi-Bouteyre, "Correcting winds measured with a Rayleigh Doppler lidar from pressure and temperature effects," *Tellus Ser. A* **60**, 206–215 (2008).
8. P. H. Flamant, A. Dabas, M. L. Denneulin, A. Dolfi-Bouteyre, A. Garnier, and D. Rees, "ILIAD: impact of line shape on ADM-Aeolus Doppler estimates," ESA Contract Final Report 1833404/NL/MM (ESTEC, 2005).
9. European Space Agency, "ADM-Aeolus," science report, ESA SP-1311 (European Space Research and Technology Centre, 2008).
10. A. Stoffelen, J. Pailleux, E. Kaellen, J. M. Vaughan, L. Isaksen, P. Flamant, W. Wergen, E. Andersson, H. Schyberg, A. Culoma, R. Meynart, M. Endemann, and P. Ingmann, "The Atmospheric Dynamics Mission for global wind field measurement," *Bull. Am. Meteorol. Soc.* **86**, 73–87 (2005).
11. D. G. H. Tan, E. Andersson, J. De Kloe, G.-J. Marseille, A. Stoffelen, P. Poli, M.-L. Denneulin, A. Dabas, D. Huber, O. Reitebuch, P. Flamant, O. Le Rille, and H. Nett, "The ADM-Aeolus wind retrieval algorithms," *Tellus Ser. A* **60**, 191–205 (2008).
12. N. Cezard, A. Dolfi-Bouteyre, J. Huignard, and P. Flamant, "Performance evaluation of a dual fringe-imaging Michelson interferometer for air parameter measurements with a 355 nm Rayleigh-Mie lidar," *Appl. Opt.* **48**, 2321–2332 (2009).
13. C. D. Boley, R. C. Desai, and G. Tenti, "Kinetic models and Brillouin scattering in a molecular gas," *Can. J. Phys.* **50**, 2158 (1972).
14. G. Tenti, C. Boley, and R. Desai, "On the kinetic model description of Rayleigh-Brillouin scattering from molecular gases," *Can. J. Phys.* **52**, 285–290 (1974).
15. M. Esselborn, M. Wirth, A. Fix, M. Tesche, and G. Ehret, "Airborne high spectral resolution lidar for measuring aerosol extinction and backscatter coefficients," *Appl. Opt.* **47**, 346–358 (2008).
16. J. Hair, L. Caldwell, D. Krueger, and C. She, "High-spectral-resolution lidar with iodine-vapor filters: measurement of atmospheric-state and aerosol profiles," *Appl. Opt.* **40**, 5280–5294 (2001).
17. J. Hair, C. Hostetler, A. Cook, D. Harper, R. Ferrare, T. Mack, W. Welch, L. Izquierdo, and F. Hovis, "Airborne high spectral resolution lidar for profiling aerosol optical properties," *Appl. Opt.* **47**, 6734–6752 (2008).
18. B. J. Rye, "Molecular backscatter heterodyne lidar: a computational evaluation," *Appl. Opt.* **37**, 6321–6328 (1998).
19. A. T. Young and G. W. Kattawar, "Rayleigh-scattering line profiles," *Appl. Opt.* **22**, 3668–3670 (1983).
20. T. J. Greytak and G. B. Benedek, "Spectrum of light from thermal fluctuations in gases," *Phys. Rev. Lett.* **17**, 179–182 (1966).
21. E. H. Hara, A. D. May, and H. F. P. Knapp, "Rayleigh-Brillouin scattering in compressed H<sub>2</sub>, D<sub>2</sub>, and HD," *Can. J. Phys.* **49**, 420–431 (1971).
22. R. P. Sandoval and R. L. Armstrong, "Rayleigh-Brillouin spectra in molecular nitrogen," *Phys. Rev. A* **13**, 752–757 (1976).
23. J. A. Lock, R. G. Seasholtz, and W. T. John, "Rayleigh-Brillouin scattering to determine one-dimensional temperature and number density profiles of a gas flow field," *Appl. Opt.* **31**, 2839–2848 (1992).
24. Q. H. Lao, P. E. Schoen, and B. Chu, "Rayleigh-Brillouin scattering of gases with internal relaxation," *J. Chem. Phys.* **64**, 3547–3555 (1976).
25. V. Ghaem-Maghami and A. D. May, "Rayleigh-Brillouin spectrum of compressed He, Ne, and Ar. I. Scaling," *Phys. Rev. A* **22**, 692–697 (1980).
26. L. Letamendia, J. P. Chabrat, G. Nouchi, J. Rouch, and C. Vaucamps, "Light-scattering studies of moderately dense gas mixtures: hydrodynamic regime," *Phys. Rev. A* **24**, 1574–1590 (1981).
27. X. Pan, M. N. Shneider, and R. B. Miles, "Coherent Rayleigh-Brillouin scattering," *Phys. Rev. Lett.* **89**, 183001 (2002).
28. X. Pan, N. Shneider, and R. Miles, "Coherent Rayleigh-Brillouin scattering in molecular gases," *Phys. Rev. A* **69**, 033814 (2004).
29. A. Sugawara and S. Yip, "Kinetic model analysis of light scattering by molecular gases," *Phys. Fluids* **10**, 1911–1921 (1967).
30. H. E. Bass, L. C. Sutherland, and A. J. Zuckerwar, "Atmospheric absorption of sound—update," *J. Acoust. Soc. Am.* **88**, 2019–2021 (1990).
31. H. E. Bass, L. C. Sutherland, J. Piercy, and L. Evans, "Absorption of sound by the atmosphere," in *Physical Acoustics*, W. P. Mason and R. N. Thurston, eds. (Academic, 1984), Vol. 17, pp. 145–232.
32. O. Reitebuch, C. Lemmerz, E. Nagel, and U. Paffrath, "The airborne demonstrator for the direct-detection Doppler wind Lidar ALADIN on ADM-Aeolus. Part I: Instrument design and comparison to satellite instrument," *J. Atmos. Oceanic Technol.* **26**, 2501–2515 (2009).
33. B. M. Gentry, H. Chen, and S. X. Li, "Wind measurements with 355 nm molecular Doppler lidar," *Opt. Lett.* **25**, 1231–1233 (2000).
34. L. Fabelinski, *The Molecular Scattering of Light* (Plenum, 1968).
35. J. P. Boon and S. Yip, *Molecular Hydrodynamics* (McGraw-Hill, 1980).
36. "U.S. standard atmosphere" (U.S. Government Printing Office, 1962).
37. T. Gombosi, *Gaskinetic Theory* (Cambridge Univ. Press, 1994).
38. N. Taxman, "Classical theory of transport phenomena in dilute polyatomic gases," *Phys. Rev.* **110**, 1235–1239 (1958).
39. C. S. Wang-Chang, G. E. Uhlenbeck, and J. de Boer, "The heat conductivity and viscosity of polyatomic gases," in *Studies in Statistical Mechanics*, J. de Boer and G. E. Uhlenbeck, eds. (North-Holland, 1964), pp. 242–268.
40. R. F. Snider, "Quantum-mechanical modified Boltzmann equation for degenerate internal states," *J. Chem. Phys.* **32**, 1051–1060 (1960).
41. W. E. Meador, G. A. Mines, and L. W. Townsend, "Bulk viscosity as a relaxation parameter: fact or fiction?," *Phys. Fluids* **8**, 258–261 (1996).
42. R. E. Graves and B. M. Argow, "Bulk viscosity: past to present," *J. Thermophys. Heat Transfer* **13**, 337–342 (1999).
43. W. A. Wakeham, "Transport properties of polyatomic gases," *Int. J. Thermophys.* **7**, 1–15 (1986).
44. G. Emanuel, "Bulk viscosity of a dilute polyatomic gas," *Phys. Fluids A* **2**, 2252–2254 (1990).
45. G. J. Prangma, A. H. Alberga, and J. J. M. Beenakker, "Ultrasonic determination of the volume viscosity of N<sub>2</sub>, CO, CH<sub>4</sub>, and CD<sub>4</sub> between 77 and 300 K," *Physica* **64**, 278–288 (1973).
46. K. Rah and B. C. Eu, "Density and temperature dependence of the bulk viscosity of molecular liquids: carbon dioxide and nitrogen," *J. Chem. Phys.* **114**, 10436–10447 (2001).
47. W. Ubachs, E.-J. van Duijn, M. O. Veitez, W. van de Water, N. Dam, J. J. ter Meulen, A. S. Meijer, J. de Kloe, A. Stoffelen, and E. A. A. Aben, "A spontaneous Rayleigh-Brillouin scattering experiment for the characterization of atmospheric lidar backscatter," ESA Contract Final Report 1-5467/07/NL/HE (ESTEC, 2009).
48. M. O. Veitez, E.-J. van Duijn, W. van de Water, and W. Ubachs are preparing a manuscript to be called "A UV laser based spectrometer for measuring spontaneous Rayleigh-Brillouin scattering."

49. G. Hernandez, *Fabry-Perot Interferometers* (Cambridge Univ. Press, 1988).
50. J. M. Vaughan, *The Fabry-Perot Interferometer* (Adam Hilger, 1989).
51. W. van de Water, A. S. Meijer, A. S. de Wijn, M. Peters, and N. J. Dam, "Coherent Rayleigh-Brillouin scattering measurements of bulk viscosity of polar and nonpolar gases, and kinetic theory," *J. Chem. Phys.* (to be published).
52. T. D. Rossing, ed., *Springer Handbook of Acoustics* (Springer, 2007).
53. D. R. Lide, ed., *CRC Handbook of Chemistry and Physics*, 82th ed. (CRC, 2002).
54. U. Paffrath, C. Lemmerz, O. Reitebuch, B. Witschas, I. Nikolaus, and V. Freudenthaler, "The airborne demonstrator for the direct-detection Doppler wind Lidar ALADIN on ADM-Aeolus. Part II: Simulations and Rayleigh receiver radiometric performance," *J. Atmos. Oceanic Technol.* **26**, 2516–2530 (2009).
55. A. Ansmann, U. Wandinger, O. Le Rille, D. Lajas, and A. Straume, "Particle backscatter and extinction profiling with the spaceborne high-spectral-resolution Doppler lidar ALADIN: methodology and simulations," *Appl. Opt.* **46**, 6606–6622 (2007).
56. M. McGill, W. Skinner, and T. Irgang, "Validation of wind profiles measured with incoherent Doppler lidar," *Appl. Opt.* **36**, 1928–1932 (1997).
57. D. Hua, M. Uchida, and T. Kobayashi, "Ultraviolet Rayleigh-Mie lidar for daytime-temperature profiling of the troposphere," *Appl. Opt.* **44**, 1315–1322 (2005).
58. J. R. Bonatto and W. Marquez, "Kinetic model analysis of light scattering in binary mixtures of monoatomic ideal gases," *J. Stat. Mech.* **9**, 09014 (2005).
59. W. van de Water, M. O. Vieitez, E.-J. van Duijn, W. Ubachs, A. Meijer, A. S. de Wijn, N. J. Dam, and B. Witschas, "Coherent and spontaneous Rayleigh-Brillouin scattering in atomic and molecular gases, and gas mixtures," *Phys. Rev. A* (to be published).